applied sciences

MDPI

Article

Improving Vertical Dimensional Accuracy in PBF-LB/M Through Artefact-Based Evaluation and Correction

Stefan Brenner * and Vesna Nedeljkovic-Groha

Institute for Design and Production Engineering, University of the Bundeswehr Munich, Werner-Heisenberg-Weg 39, 85579 Neubiberg, Germany; vesna.nedeljkovic-groha@unibw.de

* Correspondence: stefan.brenner@unibw.de

Abstract

Achieving high dimensional accuracy in the build direction remains a critical challenge in laser-based powder bed fusion of metals (PBF-LB/M), particularly for taller components. This study investigates the application of the standardized Z-artefact defined in ISO/ASTM 52902:2023 to evaluate and correct vertical dimensional deviations in AlSi10Mg parts. Benchmark artefacts were produced without Z-scaling and measured using a structured light 3D scanner. A linear trend of increasing undersizing with build height was observed across two build jobs, indicating a systematic Z-error. Based on the reproducible average deviation, a shrinkage compensation factor of 1.0017 was derived and applied in a third build job using the same processing parameters. This correction reduced the root mean square error (RMSE) from over 100 µm to below 25 µm and improved the achievable ISO tolerance grades from IT 9–11 to IT 5–9. The approach proved effective without requiring changes to process parameters. However, local surface features such as elevated edges and roughness remained dominant sources of deviation and are not captured in step height-based evaluations. Overall, this study demonstrates a practical, standard-compliant method to improve vertical dimensional accuracy in PBF-LB/M, with potential applicability to industrial quality assurance and future extension to more complex geometries.

Keywords: vertical dimensional accuracy; laser powder bed fusion (PBF-LB/M); benchmark artefact; ISO/ASTM 52902; shrinkage compensation; additive manufacturing qualification; 3D-scanning

Academic Editor: Paolo Renna

Received: 23 July 2025
Revised: 25 August 2025
Accepted: 2 September 2025
Published: 5 September 2025

Citation: Brenner, S.; Nedeljkovic-Groha, V. Improving Vertical Dimensional Accuracy in PBF-LB/M Through Artefact-Based Evaluation and Correction. *Appl. Sci.* **2025**, *15*, 9756. https://doi.org/10.3390/app15179756

1. Introduction

Laser-based powder bed fusion of metals (PBF-LB/M) is one of the most promising additive manufacturing (AM) technologies for producing complex metallic components. AM processes are increasingly adopted in key industries such as aerospace, automotive, and medical engineering due to their unique capabilities, particularly in the production of highly customized or functionally optimized parts that cannot be manufactured easily by conventional means [1]. The benefits of AM extend across multiple levels: from direct product-level advantages such as the use of lattice structures, to process chain simplification through part consolidation, to accelerated product development, and ultimately to strategic business transformation by enabling entirely new value creation models [2]. These multi-level benefits highlight the growing importance of PBF-LB/M as a manufacturing technology in industrial contexts.

With the growing industrial use of PBF-LB/M, expectations regarding part quality have risen significantly. A key focus lies on internal defects such as porosity, lack-of-fusion

voids, and cracks, all of which are known to act as stress concentrators and may lead to premature failure of components [3]. To meet these quality demands, mechanical properties and surface quality are critical performance factors. Studies have shown that parts produced via PBF-LB/M can exceed the properties of equivalent cast materials, and moreover, improved surface finish and dimensional conformity have been reported compared to cast counterparts [4]. As technical capabilities advance, repeatability and reliability become key, especially in the context of qualification and certification. In aerospace and other safety-critical industries, certification relies heavily on physical validation and often requires full-scale component testing due to the high costs of conventional qualification strategies [5]. However, the certification of metal AM parts remains challenging. Persistent issues include process variability, lack of traceability standards, and limited availability of application-specific norms and regulations [6]. These factors currently hinder the efficient qualification of AM components and highlight the need for robust, repeatable processes as well as comprehensive standards to ensure safe and cost-effective adoption.

Although PBF-LB/M is capable of producing complex metal parts with high structural integrity, maintaining tight dimensional and geometrical tolerances remains a significant challenge. One of the main reasons is the localized and intense thermal input, which leads to complex thermal histories within the part. This results in residual stresses and part deformation due to the temperature gradient mechanism (TGM) [7]. The buildup of residual stresses during laser scanning cannot be avoided entirely and has been linked to dimensional deviations, distortion, and even cracking [7,8]. In addition to thermally induced effects, dimensional accuracy is influenced by multiple factors across the digital-to-physical process chain. These include the STL generation, slicing, scan strategy, and powder consolidation during layer formation [9,10]. Even slight inaccuracies at these stages can accumulate, particularly in non-planar or inclined geometries [9,11]. While strategies like scan vector optimization can reduce residual stress, they may introduce new challenges such as local overheating and porosity [8]. Post-processing techniques like machining and abrasive finishing are used to improve the dimensional accuracy and surface finish of AM parts [12]. Studies on post-processing induced modification of dimensional and form accuracy of PBF-LB/M components are limited in the literature, and the existing post-treatment operations using laser source, chemicals, and mechanical forces exhibit limitations in ensuring desired geometrical accuracy in PBF-LB/M components [11].

It is therefore necessary to evaluate and improve the dimensional accuracy of PBF-LB/M parts in the as-built state. In several studies, simplified test geometries such as pins, cubes, and upright or flat bars are used to investigate the orientation- or position-dependent dimensional accuracy [9,13–15]. Combinations of different geometry elements are also often used to evaluate different aspects simultaneously. Liu et al. [16] used pyramid-like step models. Fotovvati et al. [17] combined squares, rods, walls, and tubes of different sizes. Brenner and Nedeljkovic-Groha [18] used cylindrical pins with truncated cone steps. Giganto et al. [19] designed different artefacts with inward-facing pockets and outward-facing pads as well as staircase-shaped surfaces. Montero et al. [20] presented an artefact design containing an array of features that can be used to determine a relative coordinate system for measurement. In a recently published review study, Maleki et al. [21] categorize seven groups of geometries and artefacts used for dimensional accuracy evaluation: single struts, lattice structures, thin walls, bulk geometries, holes and internal channels, complex geometries, and comprehensive build plates. There are several comprehensive review articles on such geometric benchmark artefacts in the literature, indicating a great variety and high interest in this type of dimensional accuracy studies and providing advice on the design of the artefacts [21–24].

A basic concept is the trade-off between evaluating the entire build volume and minimizing time and material consumption. While a balanced approach is desirable, smaller and faster test builds are often preferred due to the relatively high time and material costs associated with PBF-LB/M processes [25]. This leads to rather flat artefact designs that allow for dimensional accuracy evaluation in the XY plane, but rarely along the *z*-axis. Studies on artefacts with high build heights are scarce [20,21,26,27] or deal with AM processes other than PBF-LB/M [28].

In order to meet the challenges in a structured manner, standardization was driven forward [6,29], and the standard ISO/ASTM 52902 was introduced for the general description of benchmarking artefacts for evaluating the performance of AM systems. The standard defines several types of artefacts designed to verify specific aspects of AM performance, including accuracy, resolution, surface texture, and part labeling. The most significant update from the original 2019 version to the current 2023 revision is the addition of a dedicated artefact for the evaluation of the accuracy in the z-direction [30]. However, there is currently only a limited number of studies addressing the application and practical relevance of the artefacts defined in ISO/ASTM 52902. A literature search conducted in the Scopus database [31] (latest search date: mid-July 2025) using the query string 52902 AND (artifact OR artefact OR "test piece" OR benchmark) yielded 27 documents. Among these, only a subset explicitly discusses the use of the artefacts and procedures described in ISO/ASTM 52902. Most studies base the characterization of surface roughness on the guidelines of the standard [32–37]. Berez et al. [32] and Krasniqi et al. [34] additionally use linear and circular artefacts for the accuracy assessment of the PBF-LB/M process in the XY plane as well as resolution artefacts but do not perform height measurements in the z-direction. Grabe et al. [35] use an adapted linear benchmark geometry to evaluate the accuracy of the Multi-Jet Modeling (MJM) process when printing a photopolymer in x-, y-, and z-directions. Monzón et al. [36] measure the heights of resolution pin artefacts from copper fabricated via a filament-based material extrusion process called Atomic Diffusion Additive Manufacturing (ADAM). Spitaels et al. [37] adapted a geometrical benchmark test artefact from [25] for Fused Deposition Modelling (FDM) with PLA, while Flierl et al. [38] adapted it to vat photopolymerization. Both studies investigated the dimensional accuracy, including step heights of staircase features. To the authors' knowledge, the *z*-axis artefact introduced in ISO/ASTM 52902:2023 [30] (hereinafter: Z-artefact) has not yet been investigated in any published research. Given the current lack of systematic investigations into the dimensional accuracy of AM systems in the build direction, this new Z-artefact offers the first standardized approach for analyses along the build height. It fills an important gap in the existing set of artefacts, which primarily focus on evaluations perpendicular to the build direction. Its simple geometry, a solid body with vertical walls and staircase features, makes it easy to measure using optical or tactile systems. The standard provides detailed specifications for datum planes to ensure reproducibility and comparability, which is essential for industrial applicability and for establishing consistent quality benchmarks in industrial AM processes. Optionally proposed flatness assessments of the side surfaces offer additional insights, even at high build heights.

In this study, we fabricate and evaluate the Z-artefact as specified in ISO/ASTM 52902:2023, using the PBF-LB/M process with AlSi10Mg as build material. AlSi10Mg is a widely used and industrially relevant alloy in additive manufacturing. According to the material database of commercially available finite element (FE) software, it has the highest coefficient of thermal expansion (CTE) among common PBF-LB/M alloys such as Ti-6Al-4V, In718, and 316L [39]. This makes it particularly susceptible to thermal shrinkage, which is central to this investigation. Multiple artefacts from different build jobs were measured repeatedly to investigate reproducibility and assess systematic height deviations in the

artefacts. Based on the measurement data, we propose a practical correction approach using a scaling factor to compensate for build height errors and demonstrate that this method significantly improves vertical dimensional accuracy. Our findings underline the potential of this standardized artefact to support process optimization, which contributes to improved part quality, reduced post-processing effort, and higher profitability by minimizing scrap.

2. Materials and Methods

2.1. Test Specimen Fabrication

AlSi10Mg powder with a particle size distribution of 20–63 µm, according to the supplier's data sheet [40] (Nikon SLM Solutions AG, Lübeck, Germany), was used in this study. The powder consisted of a blend of virgin and used powder in condition 2B, as defined in VDI guideline 3405, Part 2.6 [41].

For the fabrication of the artefacts, a commercially available SLM®125 PBF-LB/M system from Nikon SLM Solutions with a silicone rubber recoater lip was used. The system is equipped with an image-based Layer Control System (LCS) that monitors the quality of powder spreading for each powder layer. The main processing parameters are given in Table 1. No heat treatment or other post-processing steps were performed.

Table 1. Main PBF-LB/M process parameters for AlSi10Mg.

Parameter	Volume	Border
Laser power (W)	350	300
Scan speed (mm/s)	1650	730
Hatch distance (mm)	0.13	-
Stripe rotation angle after each layer (°)	67	-
Layer thickness (µm)	30	
Baseplate temperature (°C)	150	
Inertization	Ar 4.6 (oxygen content < 500 ppm)	

The build jobs were prepared using the software Magics 25.04 (Materialise NV, Leuven, Belgium). As a default, no scaling of the CAD model in the build direction (shrinkage compensation factor SCF_z = 1.00) was applied, as the PBF-LB/M process is generally assumed to inherently compensate for vertical shrinkage through the recoating and remelting mechanism during layer-by-layer fabrication [27]. The artefacts were oriented so that their outer edges were aligned at a 45° angle relative to the recoater movement, which was bidirectional along the *y*-axis. No remelting of horizontal surfaces was applied. It should be noted that in addition to the Z-artefacts, the build jobs also included other parts that are not related to this study.

The medium-sized artefact variant proposed in ISO/ASTM 52902:2023 was selected for this study. It features 16 steps with 5 × 5 mm^2 horizontal surfaces and a total height of 99.5 mm, including a 2 mm base section (Figure 1a). This variant was chosen as it efficiently utilizes the available build volume of the SLM®125 system. A fundamental design aspect is the uneven spacing of the step heights, which are not necessarily multiples of the layer thickness. The tops of the steps can therefore be located between the individual layer heights. Note: the artefacts used in the first two build jobs (labeled A to D) exhibit a minor deviation from the ISO/ASTM 52902:2023 geometry. The four tallest steps were arranged in reverse order, while their nominal heights remained unchanged. This design variation has no influence on the intended purpose or the evaluation of the *z*-axis performance, but the standardized design will be used for further build jobs in this study. It should also be noted that an inconsistency was identified in ISO/ASTM 52902:2023 regarding the nominal height of the second-highest step: while the technical drawing in the standard specifies 94.0 mm,

the corresponding value in the tabulated data is 94.5 mm. In this work, the tabulated value of 94.5 mm is used.

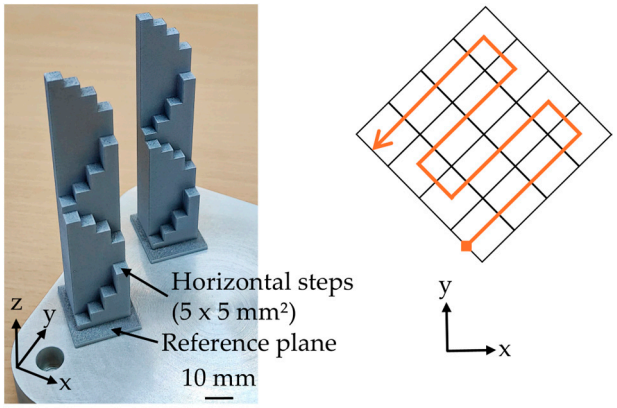

Figure 1. (**a**) AlSi10Mg examples of the Z-artefacts according to ISO/ASTM 52902:2023 [30] on the baseplate matted with scanning spray for optical measurement; (**b**) schematic measurement profile path.

2.2. 3D Scanning and Evaluation

The Z-artefacts were measured using two optical systems: a structured light 3D scanner (Keyence VL-550, Keyence Co., Osaka, Japan [42]) and an optical 3D profilometer (Keyence VR-5200, [43]). The 3D scanner was used in low-magnification mode with the super fine measurement setting, offering a measurement accuracy of ±10 µm and a repeatability of 2 µm. Each baseplate with the artefacts attached to it was scanned from 12 directions using a 30° stage rotation between each view. These single scans were automatically merged by the Keyence VL-550 V2.3.8.85 software to generate a complete 3D model of the assembly. Prior to the measurements, the 3D scanner was calibrated using the certified Keyence calibration board OP-88145. To verify the system performance, 20 repeated measurements were conducted using the Keyence calibration ball gauge VL-B1 for the xy-directional validation and the Keyence standard ceramic block OP-88275 for the z-direction. The deviations from the certified reference values remained below 10 µm in all directions. For detailed surface analysis, the 3D profilometer was operated in high-resolution mode (80× magnification) without Z-stitching, enabling the analysis of individual step topographies with the best possible measurement accuracy (height: ±2.5 µm, width: ±2.0 µm) and repeatability (height: 0.4 µm, width: 0.5 µm). The maximum height surface roughness Sz was evaluated using an L-filter with a cutoff wavelength of 0.8 mm as in [11], but using larger measurement areas of 4 × 4 mm^2. Due to the limited working distance, only steps 4 to 7 could be captured using the 3D profilometer. To prevent light reflections, the baseplate and the artefacts were coated with a thin layer of the scanning spray (“induscan spray”, Dentaco GmbH, Essen, Germny) [44]. According to the supplier, the coating thickness is less than 5 µm.

Each artefact was scanned three times using the 3D scanner, and the data were processed in the Keyence VL-550 software using a predefined analysis template to ensure user-independent and reproducible evaluation. The step heights analysis was carried out by defining the top surface of the base of the artefact as the reference plane and performing a profile measurement along the centerline of the stair geometry (see Figure 1b). At each step, a best-fit line was applied to the measured profile. The midpoint of each fitted line was evaluated as the vertical distance to the reference plane, corresponding to an averaged step height. Local height deviations, such as elevated outer edges, were excluded from the

analysis. To assess manufacturing repeatability, two identical build jobs were performed, each containing two artefacts, as exemplified in Figure 1a).

Step height errors were obtained by subtracting the nominal heights from the measured values. Negative errors correspond to undersized steps relative to the CAD model, while positive errors indicate oversize. The complete dataset of uncompensated build jobs (SCF_z = 1.00) includes four artefacts (A to D) with three repeated measurements, resulting in 192 values in total. To quantify the overall vertical dimensional accuracy, the root mean square error (RMSE) was calculated for each artefact based on the 16 step height errors and three repetitions:

$$\mathrm{RMSE} = \sqrt{\frac{1}{n}\sum_{i=1}^{n}(h_i - h_{CAD,i})^2}, \quad (1)$$

where h_i is the measured step height, $h_{CAD,i}$ is the corresponding nominal height, and n = 48 is the total number of measurements per artefact. To support statistical interpretation, the RMSE is reported together with the 95% confidence interval (95% CI), which is calculated from the mean value ± 1.96 times the standard error of the same data. Unlike the RMSE, which is always positive, the 95% CI retains the sign of the underlying deviation.

The analysis of the first two build jobs focuses on identifying systematic error trends. If a linear deviation along the *z*-axis is observed, an adjustment of the SCF_z may be considered. Should this correction strategy show promising potential for improving dimensional accuracy, a third build job will be carried out to validate its effectiveness.

To illustrate the differences in resolution and surface detail between the two optical measurement systems, Figure 2 shows false color height plots of a representative step surface captured with the 3D profilometer (80× magnification, Figure 2a) and the 3D scanner (Figure 2b). The 3D profilometer measurements reveal finer topographical features such as elevated edges, individual scan tracks, adhering powder particles, and local recesses. In contrast, the 3D scanner smooths the surface topography due to its lower resolution but still provides sufficient detail for evaluating the dimensional accuracy.

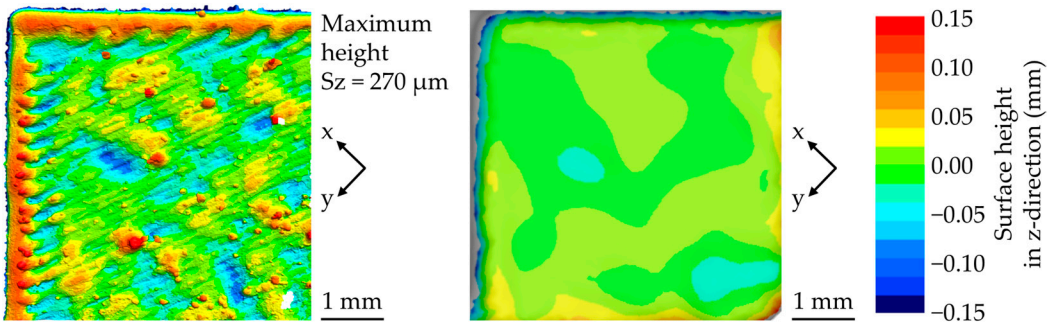

Figure 2. Surface topography of an exemplary 5 × 5 mm^2 step captured with different optical systems: (**a**) 3D profilometer VR-5200 (80× magnification, high-resolution mode); (**b**) 3D scanner VL-550 (low magnification, super fine measurement mode). The maximum height Sz is 270 µm, averaged from 4 × 4 mm^2 measurement areas on several step surfaces. Elevated edges (red borders in (**a**)) were excluded from the evaluation.

ISO/ASTM 52902:2023 suggests checking the flatness of the vertical side faces of the artefact as an optional evaluation. In this study, we analyze the flatness of the rear wall, which is the largest and most informative surface, with an area of approximately 1826 mm^2. The evaluation is performed using the flatness analysis function of the Keyence VL-550 software. The flatness of this vertical surface directly influences the dimensional accuracy perpendicular to the build direction, i.e., in the XY plane. Only if the flatness deviation is small does a constant scaling offer a reasonable prospect of correcting potential dimensional

inaccuracies in the XY plane. Furthermore, a significant curvature would indicate that simple linear scaling is not sufficient and that alternative correction strategies would be needed, which are not addressed in this work.

3. Results

3.1. Unscaled Artefacts

From the first two build jobs, which were conducted without any scaling in the build direction (SCF_z = 1.00), a total of 192 step height measurements were obtained using the 3D scanner (Keyence VL-550). These include 16 steps on each of the four artefacts (A to D), with three repeated scans per artefact. Figure 3 presents the corresponding absolute step height errors for all individual measurements.

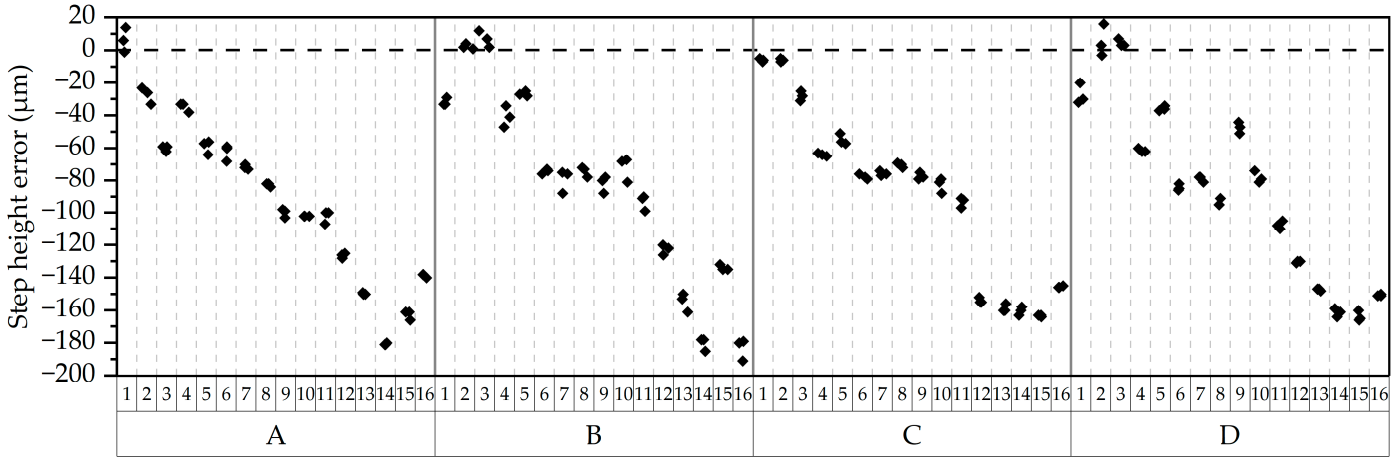

Figure 3. Absolute step height errors of steps 1 to 16 of each unscaled Z-artefact (A and B from build job 1, C and D from build job 2). For each individual step, three measurement repetitions are shown.

The three lowest steps exhibit considerable variation, with deviations between −62 µm and 16 µm. As the step height increases, the errors tend to decrease approximately linearly into the negative range, reaching values below −160 µm at the highest steps. The repeatability of the measurements is high, as indicated by the low dispersion among the three repetitions per step. The largest observed scatter is 19 µm, occurring at step 2 in artefact D. Notably, 83% of all measurement triplets deviate by less than 10 µm, and 52% show deviations below 5 µm.

Based on the results presented above, the vertical dimensional accuracies were quantified as $RMSE_A$ = 104 µm (95 % CI: −105 to −76 µm), $RMSE_B$ = 101 µm (95 % CI: −100 to −67 µm), $RMSE_C$ = 103 µm (95 % CI: −103 to −74 µm), and $RMSE_D$ = 101 µm (95 % CI: −100 to −69 µm). The RMSE values are very similar across all Z-artefacts, indicating a highly consistent dimensional performance between the two build jobs and among the individual artefacts. Figure 4 shows the same step height errors as in Figure 3, but now presented as boxplots relative to the nominal step heights. Each boxplot represents a total of 12 relative step height error values, derived from Z-artefacts A to D with three repeated measurements each.

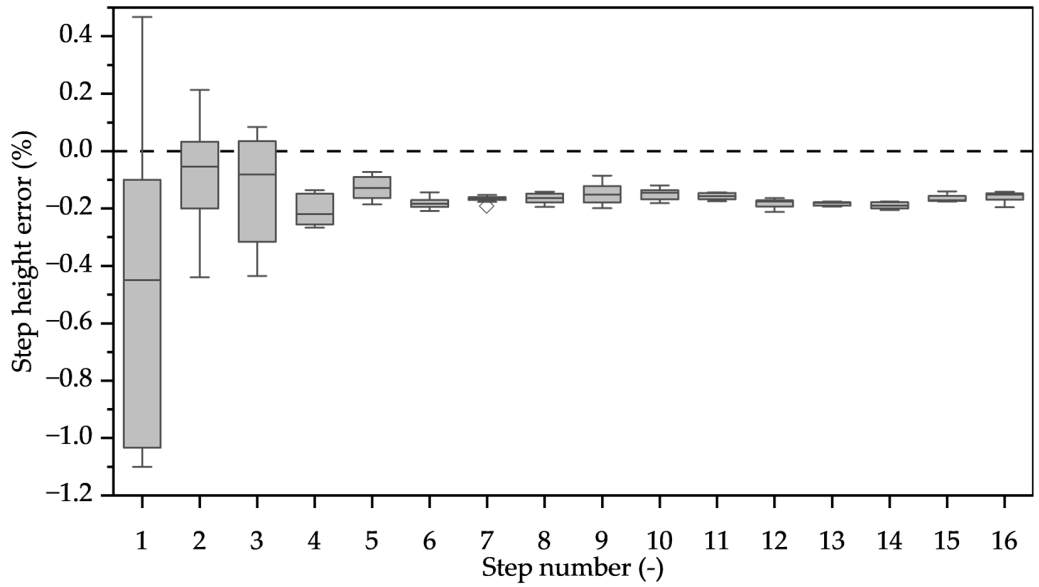

Figure 4. Boxplots with median lines of the relative step height errors for all 16 steps of unscaled artefacts A to D. Each boxplot represents 12 values obtained from Z-artefacts A to D and three repeated measurements per Z-artefact. One outlier value (diamond symbol at step 7) is present.

A greater spread is observed in the lower steps, as indicated by the larger boxes and whiskers. From step 4 onward, the relative step height errors converge around an average of −0.168%, with a 95% confidence interval ranging from −0.173% to −0.163%.

3.2. Z-Scaled Artefacts

The observed systematic undersizing in the z-direction suggests potential for optimization. A compensation strategy based on a modified shrinkage factor (SCF_z) appears promising to reduce the global dimensional deviation while maintaining repeatability. To achieve this, two additional artefacts (E and F) were fabricated in a third build job. A scaling factor of SCF_Z = 1.0017 was applied during the pre-processing, based on the highly reproducible average undersizing of −0.168% observed in steps 4 to 16 of the initial (unscaled) artefacts. The standardized design of the artefacts from ISO/ASTM 52902:2023 was used for this build job. Figure 5 shows the absolute step height errors for all individual measurements from the Z-scaled (SCF_Z = 1.0017) artefacts E and F.

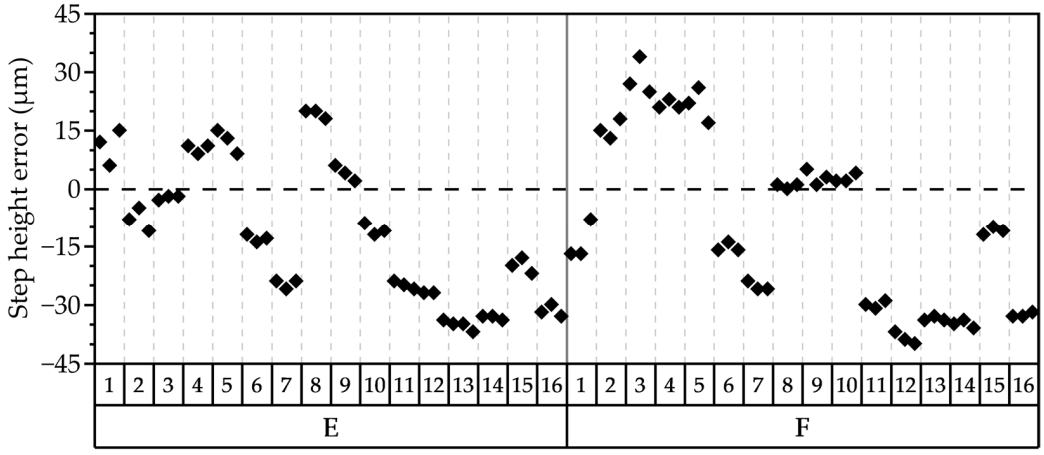

Figure 5. Absolute step height errors of the 16 steps of the Z-scaled artefacts E and F (SCF_Z = 1.0017) from build job 3. For each step, three repeated measurements are shown.

All step height errors are centered around zero, ranging from −40 µm to 34 µm. While a slight overcompensation is observed at the lower steps, a minor tendency toward undersizing remains at the highest steps. In Figure 6, absolute step height errors (black) and relative errors (red) are shown as boxplots and individual data points for both unscaled and the Z-scaled artefacts. The boxplots for the Z-scaled artefacts show that the error value of zero is within their interquartile ranges, indicating that the majority of the measured deviations are close to the nominal values. The average relative error is −0.005% (median: −0.026%) after Z-scaling.

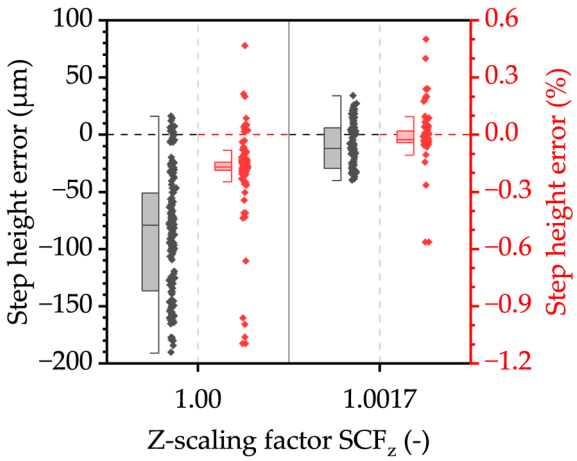

Figure 6. Boxplots with median lines and data points of all measured step height errors for the unscaled artefacts A–D (SCF_Z = 1.00) and the Z-scaled artefacts E and F (SCF_Z = 1.0017), shown as absolute errors (black) and relative errors (red).

The vertical dimensional accuracies were substantially improved to values of $RMSE_E$ = 21 µm (95 % CI: −16 to −6 µm) and $RMSE_F$ = 24 µm (95 % CI: −15 to −3 µm), which are smaller than one layer thickness. This demonstrates that the applied scaling factor effectively compensates for the systematic z-direction error. By applying the Z-scaling factor, the achievable International Tolerance (IT) grades according to the ISO 286-1:2019 guideline [45] improved from $9 \leq IT \leq 11$ (artefacts A to D) to $5 \leq IT \leq 9$ (artefacts E and F), with individual step tolerances improving by 1 to 5 IT grades depending on the step height. It should be noted that this assessment is based on averaged step height deviations and does not account for local surface effects such as elevated edges or roughness peaks, which may exceed the evaluated tolerances under both unscaled and scaled conditions.

3.3. Flatness of Vertical Side Faces

As specified in ISO/ASTM 52902:2023, the Z-artefact offers additional optional measurement features, such as the form of the vertical surfaces. Height maps were created to visualize the deviation of the surfaces perpendicular to the z-direction in Figure 7a–f. The diagram in Figure 7g presents the mean values and standard deviations of the flatness tolerances of Z-artefacts A to F.

The rear wall exhibits a concave curvature, with positive deviations at the top and bottom and negative deviations in the center. It is noticeable that the largest positive form deviation occurs at the very bottom of the surface (orange to red color), extending up to a height of approximately 8 mm. Including these deviations, the flatness mean values range between 110 µm and 145 µm, as shown in Figure 7g. When the first 8 mm are excluded, the flatness improves, with mean values ranging between 73 µm and 91 µm. The largest standard deviations, 33 µm for artefact B and 16 µm for artefact F, also decrease when the bottom section is excluded.

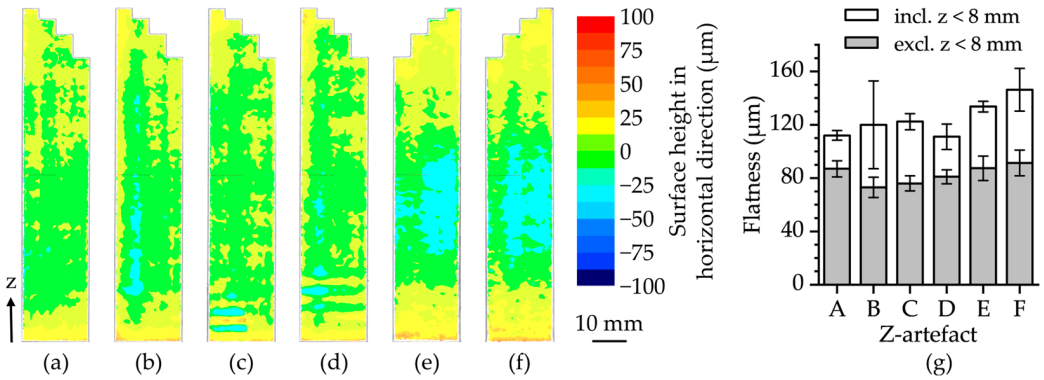

Figure 7. (**a**–**f**) Height maps of the rear wall surfaces of Z-artefacts A to F. (**g**) Mean values with error bars (±1 × standard deviation) of the flatness tolerances of Z-artefacts A to F from three repeated measurements (n = 3). White columns represent the entire surface area; gray columns represent the surface area excluding the lower region of z < 8 mm.

4. Discussion

4.1. Repeatability and Systematic Error Trends

By producing two identical artefacts in each build job and repeating the 3D-scanning process three times, high measurement and manufacturing repeatability between and within build jobs were demonstrated. Although the 3D scanner specifies a repeatability of 2 µm, this applies to ideal ceramic gauges. The textured, spray-coated surfaces of PBF-LB/M parts are more challenging, yet 52% of all triple measurement repetitions show deviations of less than 5 µm, demonstrating high repeatability under practical conditions. The limited resolution of the 3D scanner did not compromise the reliability of the dimensional accuracy evaluation in this context.

A linear progression of undersizing, at least above a certain build height, indicated a systematic Z-error trend for AlSi10Mg. This finding was also reported by Yasa et al. [27], who identified thermal shrinkage as the cause, which can be compensated for. Silva et al. [46] also observed slightly undersized staircase heights, but attributed this to positioning errors of the machine's z-axis or surface roughness. However, Lu et al. [47] report on an experiment with a PFB-LB/M system in which the position error of the platform over a distance of 150 mm is approximately 4.5 µm, which is two orders of magnitude smaller than the z-deviations determined by Silva et al. Therefore, it is more likely that the undersizing is due to shrinkage caused by a coefficient of thermal expansion (CTE) of AlSi10Mg of 23.5 ppm/°C, valid between room temperature and 350 °C [48].

The RMSE values across all unscaled artefacts range narrowly between 101 µm and 104 µm, indicating consistent vertical dimensional performance with the potential for improvement through shrinkage compensation.

4.2. Effectiveness of Z-Scaling Compensation

The application of a Z-scaling factor (SCF_Z = 1.0017) led to a substantial improvement in vertical dimensional accuracy. This value was obtained for AlSi10Mg under the specific process conditions used in this study and may not be directly applicable to other material–machine combinations. The SCF_Z value was derived from the relative step height errors from step 4 onwards, which have a narrow 95% confidence interval of −0.173% to −0.163%. Therefore, the sensitivity of the method to slight variations in the SCF_Z is considered to be low. The RMSE values for the Z-scaled artefacts E and F were reduced by 75% to 21 µm and 24 µm, respectively, resulting in an average relative error of only −0.005%. The achievable IT grades improved from IT 9–11 to IT 5–9. To illustrate the degree of accuracy achieved

in the general manufacturing context, reference is made to an IT 10 requirement for the blanking process of parts for medical technology applications [49].

However, local surface topography features such as adhering powder, elevated edges (up to 80–90 µm) as well as high surface roughness (Sz ≈ 270 µm) exceed the remaining step height deviations after compensation. These irregularities, clearly visible in the 3D profilometer topography (Figure 2a), are significantly larger than the average step height errors and may lead to misleading conclusions if IT grades are interpreted without considering local surface deviations, which are not captured in the step height evaluation. By adjusting the process parameters and using remelting scan strategies, edge effects and roughness can be reduced, thereby improving the flatness of horizontal surfaces [9,50,51] or directly improving the dimensional accuracy [9,52]. However, even the reduced elevated edges reported in the literature after process parameter optimization are typically larger than the step height errors observed for the Z-scaled artefacts in this study. In contrast, Zhang et al. [13] found no significant influence of process parameters such as scan speed, hatch distance, and laser power on the vertical dimensional accuracy of Ti6Al4V samples. In this study, the approach was to leave the process parameters (see Table 1) unchanged and to achieve an improvement in vertical dimensional accuracy solely through a geometry scaling factor. This is particularly advantageous for the production of parts in regulated industries where approved process parameter sets are used, which might otherwise have to undergo a costly re-qualification procedure [53]. Other possible causes of local quality problems in components are irregularities in the powder bed. Uneven powder distribution, such as grooves and streaks, can lead to microstructural defects, increased surface roughness, and deviations in dimensional accuracy [54,55]. We reviewed the LCS images for all layers of all build jobs and found uniform and consistent powder distribution. Based on this, we consider the influence of irregularities in the powder bed on the Z-deviations observed in this study to be negligible.

4.3. Limitations

Despite the overall improvement, some limitations of the Z-scaling approach were identified. In some of the lower steps, there was slight overcompensation, while in the highest steps, a slight tendency toward undersizing remained.

Since the layer heights are intentionally not exact multiples of the layer thickness, discretization errors of up to ±0.5 times the layer thickness (±15 µm in this study) can occur during slicing. ISO/ASTM 52902:2023 explicitly recommends verifying how the slicing software handles these effects and incorporating this into the evaluation. An analysis of the sliced build job files for the unscaled artefacts revealed that most step levels, including the reference level, were positioned at +10 µm relative to the ideal CAD geometry, while steps 4 and 12 were rounded to −5 µm. Consequently, these two steps have a discretization error of −15 µm relative to the reference plane. For all other steps, the effect of discretization is uniform and does not contribute to the measured deviations in step height errors.

Another potential factor influencing the observed scatter is the presence of additional parts, not related to this study, in the build jobs. These parts were flatter but had a considerable cross-sectional area, which increased the scan time per layer and prolonged the local dwell time between layers. It is to be expected that longer solidification times can lead to greater shrinkage in the vertical direction [52]. In build jobs 1 and 2, the Z-artefacts accounted for only ~16% of the total layer area up to step 2, increasing to 26% at step 3 and 88% at step 4, after which the adjacent parts were completed. In build job 3, adjacent parts with constant cross-sections were finished between steps 10 and 11, where the artefacts made up ~44% of the layer area. Layers with larger exposure areas may have allowed for a longer cooling time, while shorter layer cycles may have limited cooling

and slightly increased residual heat. Although this effect is secondary compared to the systematic Z-deviation, it may contribute to the increased scatter observed in the lower levels of uncompensated artefacts. Morvayova et al. [56] demonstrated in a numerical and experimental study that adjacent parts can cause an uneven heat distribution across the baseplate, leading to increased dimensional errors, particularly in parts located near the baseplate edges. In our study, the artefacts were likewise positioned close to the edge of the baseplate. It may therefore be assumed that the presence of adjacent parts contributed to the observed variation in dimensional accuracy, especially at the lower step heights.

Regarding the improvement of horizontal dimensional accuracy (perpendicular to the build direction), a linear scaling approach in the XY plane appears to offer only limited potential and was therefore not pursued further in this study. The flatness analysis revealed a concave curvature of the artefacts along the height of the structure. This type of deviation is unlikely to be corrected by scaling, as such adjustments would merely stretch or compress the existing geometry in the XY plane without correcting the underlying distortion. The observed curvature is presumably caused by thermal deformation during the PBF-LB/M process. More advanced approaches such as finite element simulations may be necessary to predict and compensate for such effects. The feasibility of these methods was already demonstrated several years ago at technology readiness level (TRL) 5–6 [57]. Nevertheless, the correction of dimensional deviations that may not be sufficiently addressed through scaling is beyond the scope of this study.

The rotation around the *z*-axis of all Z-artefacts in this study was set to 45° relative to the recoater movement (y-direction, bidirectional) and the shielding gas flow in negative x-direction. The influence of the part rotation and related direction-dependent effects on possible anisotropic material behavior was not investigated but is expected to be minor due to the applied rotating stripe scan strategy, which is intended to reduce direction-dependent behavior in the XY plane [58].

To enable accurate optical measurements, the artefacts were coated with scanning spray. The influence of the spray layer thickness on the step height measurements was neglected, as it is smaller than the 3D-scanner's measurement accuracy and negligible compared to the surface roughness (Sz = 270 µm, Figure 2a), which is approximately two orders of magnitude greater.

4.4. Implications for Qualification and Future Research

The results underscore the value of artefact-based AM process evaluation in accordance with ISO/ASTM 52902:2023. The dedicated Z-artefact enables systematic evaluation of vertical accuracy and the identification and correction of systematic build errors. By combining this standardized geometry with a practical compensation approach, this work presents a methodology that contributes to dimensional quality assurance and is potentially relevant for qualification strategies in regulated applications. The Z-artefact may also serve as a standardized test specimen in the context of Factory Acceptance Testing (FAT), Site Acceptance Testing (SAT), Process Qualification (PQ), and revalidation procedures as defined in ISO/ASTM TS 52930:2021 [59], which are highly relevant for industries with strict quality requirements.

Further studies should investigate whether the presented method can be transferred to more complex and application-oriented geometries. In particular, free-form surfaces, topology-optimized structures, and lattice geometries, which are characteristic of AM, should be given greater consideration. Corresponding benchmark artefacts have already been proposed in the literature [21,24,60,61], but their dimensional behavior and suitability for systematic correction strategies remain largely unexplored. The cross-sectional changes typical of complex geometries can lead to additional thermally induced deformations

in the XY plane [62,63], which have also been observed in test artefacts [64]. In larger builds, anisotropic thermal behavior may further influence dimensional deviations. While Z-directional shrinkage appeared approximately linear in this study, curvature effects in the XY plane may increase nonlinearly with build height. Such effects should be taken into account when designing artefacts based on ISO/ASTM 52902:2023 for broader applicability.

An additional potential design modification to reduce the influence of elevated edges could be the addition of chamfers to the edges of horizontal surfaces where height measurements are taken. To investigate the robustness and transferability of the concept, experiments should also be conducted under different environmental conditions and with different PBF-LB/M systems. Further investigations into thermal deformations and the interactions of adjacent parts on the baseplate require thermal and thermomechanical modeling and simulation.

5. Conclusions

This study demonstrates the effectiveness of a standardized, benchmark artefact-based evaluation method for detecting and correcting deviations in build height in laser-based powder bed fusion of metals (PBF-LB/M). Using the reference artefact defined in ISO/ASTM 52902:2023 for the evaluation of the *z*-axis and AlSi10Mg as the building material, the following key results were achieved:

1. High measurement and manufacturing repeatability was confirmed in two build jobs, with 52% of all three times repeated measurements showing deviations of less than 5 µm.
2. Above a certain height range, systematic undersizing in the build direction was observed, indicating a linear trend due to thermal shrinkage.
3. By applying a shrinkage compensation factor in the z-direction (SCF_Z) of 1.0017, the achievable IT grades based on averaged step height values were improved from IT 9–11 to IT 5–9. However, this classification does not take into account local dimensional deviations such as elevated edges or surface roughness, which may exceed the specified tolerances.
4. The remaining deviations ranged from −40 µm to 34 µm, with a root mean square error (RMSE) below the 30 µm layer thickness, which underscores the effectiveness of the correction strategy.
5. Limitations in improving the vertical dimensional accuracy arise from layer discretization, local surface effects (e.g., roughness, elevated edges), and possible thermal variations due to the arrangement of adjacent parts in the build volume. Layer discretization errors are intentionally introduced and should be carefully considered during evaluation. To mitigate elevated edge effects without modifying process parameters, a design-based suggestion has been proposed. The thermal influence of adjacent parts should also be taken into account, which could be further investigated through simulation.
6. The approach does not require any changes to process parameters and is therefore suitable for regulated industries that rely on prequalified parameter sets.
7. The standardized Z-artefact is suitable for detecting and correcting build-height-dependent dimensional deviations and may support Factory Acceptance Tests (FATs), Site Acceptance Tests (SATs), and Process Qualification (PQ) in the context of qualification and revalidation processes in regulated AM environments.
8. Further studies should address application-oriented geometries, transferability to other systems and materials, and thermomechanical simulations to investigate the effects of thermal deformation.

Author Contributions: Conceptualization, S.B. and V.N.-G.; methodology, S.B.; software, S.B.; validation, S.B. and V.N.-G.; formal analysis, S.B. and V.N.-G.; investigation, S.B.; resources, S.B. and V.N.-G.; data curation, S.B.; writing—original draft preparation, S.B.; writing—review and editing, S.B. and V.N.-G.; visualization, S.B.; supervision, V.N.-G.; project administration, V.N.-G.; funding acquisition, V.N.-G. All authors have read and agreed to the published version of the manuscript.

Funding: This research was funded by "dtec.bw—Digitalization and Technology Research Center of the Bundeswehr" (project: FLAB-3Dprint), which we gratefully acknowledge. dtec.bw is funded by the European Union—NextGenerationEU. We also acknowledge financial support by Universität der Bundeswehr München.

Institutional Review Board Statement: Not applicable.

Informed Consent Statement: Not applicable.

Data Availability Statement: The original contributions presented in this study are included in the article. Further inquiries can be directed to the corresponding author.

Acknowledgments: The authors would like to thank our student Nikolas Koch for his support in CAD design and calibration of the measuring instruments.

Conflicts of Interest: The authors declare no conflicts of interest.

Abbreviations

The following abbreviations are used in this manuscript:

PBF-LB/M	Laser-based Powder Bed Fusion of Metals
RMSE	Root Mean Square Error
AM	Additive Manufacturing
MJM	Multi-Jet Modeling
ADAM	Atomic Diffusion Additive Manufacturing
FDM	Fused Deposition Modelling
SCF	Shrinkage Compensation Factor
FAT	Factory Acceptance Test
SAT	Site Acceptance Test
PQ	Process Qualification

References

1. DebRoy, T.; Wei, H.L.; Zuback, J.S.; Mukherjee, T.; Elmer, J.W.; Milewski, J.O.; Beese, A.M.; Wilson-Heid, A.; De, A.; Zhang, W. Additive manufacturing of metallic components–Process, structure and properties. *Prog. Mater. Sci.* **2018**, *92*, 112–224. [CrossRef]
2. Schneck, M.; Gollnau, M.; Lutter-Günther, M.; Haller, B.; Schlick, G.; Lakomiec, M.; Reinhart, G. Evaluating the Use of Additive Manufacturing in Industry Applications. *Proced. CIRP* **2019**, *81*, 19–23. [CrossRef]
3. Zhang, B.; Li, Y.; Bai, Q. Defect Formation Mechanisms in Selective Laser Melting: A Review. *Chin. J. Mech. Eng.* **2017**, *30*, 515–527. [CrossRef]
4. Pratap Singh, S.; Kumar Gupta, R.; Agarwal, A.; Govind. Processing and characterization of Al-Si-Mg alloy made through 3D printing and comparison with equivalent cast alloy. *Mater. Today Proc.* **2022**, *67*, 422–430. [CrossRef]
5. Venturi, F.; Taylor, R. Additive Manufacturing in the Context of Repeatability and Reliability. *J. Mater. Eng. Perform.* **2023**, *32*, 6589–6609. [CrossRef]
6. Chen, Z.; Han, C.; Gao, M.; Kandukuri, S.Y.; Zhou, K. A review on qualification and certification for metal additive manufacturing. *Virtual Phys. Prototyp.* **2022**, *17*, 382–405. [CrossRef]
7. Zaeh, M.F.; Branner, G. Investigations on residual stresses and deformations in selective laser melting. *Prod. Eng. Res. Devel.* **2010**, *4*, 35–45. [CrossRef]
8. Mugwagwa, L.; Dimitrov, D.; Matope, S.; Yadroitsev, I. Investigation of the effect of scan vector length on residual stresses in selective laser melting of maraging steel 300. *S. Afr. J. Ind. Eng.* **2019**, *30*, 60–70. [CrossRef]
9. Cao, L.; Li, J.; Hu, J.; Liu, H.; Wu, Y.; Zhou, Q. Optimization of surface roughness and dimensional accuracy in LPBF additive manufacturing. *Opt. Laser Technol.* **2021**, *142*, 107246. [CrossRef]

10. Calignano, F. Investigation of the accuracy and roughness in the laser powder bed fusion process. *Virtual Phys. Prototyp.* **2018**, *13*, 97–104. [CrossRef]
11. Boban, J.; Ahmed, A. Electric discharge aided surface post-treatment of laser powder bed fused non-planar metallic components for enhanced form accuracy. *J. Manuf. Process.* **2024**, *109*, 564–582. [CrossRef]
12. Peng, X.; Kong, L.; Fuh, J.Y.H.; Wang, H. A Review of Post-Processing Technologies in Additive Manufacturing. *J. Manuf. Mater. Process.* **2021**, *5*, 38. [CrossRef]
13. Zhang, L.; Zhu, H.; Zhang, S.; Wang, G.; Zeng, X. Fabricating high dimensional accuracy LPBFed Ti6Al4V part by using bi-parameter method. *Opt. Laser Technol.* **2019**, *117*, 79–86. [CrossRef]
14. Ahmed, A.; Majeed, A.; Atta, Z.; Jia, G. Dimensional Quality and Distortion Analysis of Thin-Walled Alloy Parts of AlSi10Mg Manufactured by Selective Laser Melting. *J. Manuf. Mater. Process.* **2019**, *3*, 51. [CrossRef]
15. Giorgetti, A.; Ceccanti, F.; Baldi, N.; Kemble, S.; Arcidiacono, G.; Citti, P. Axiomatic Design of a Test Artifact for PBF-LM Machine Capability Monitoring. *Machines* **2024**, *12*, 199. [CrossRef]
16. Liu, Y.; Yang, Y.; Wang, D. Investigation into the shrinkage in Z-direction of components manufactured by selective laser melting (SLM). *Int. J. Adv. Manuf. Technol.* **2017**, *90*, 2913–2923. [CrossRef]
17. Fotovvati, B.; Asadi, E. Size effects on geometrical accuracy for additive manufacturing of Ti-6Al-4V ELI parts. *Int. J. Adv. Manuf. Technol.* **2019**, *104*, 2951–2959. [CrossRef]
18. Brenner, S.; Nedeljkovic-Groha, V. Enhancing Dimensional Accuracy in Laser Powder Bed Fusion by Scaling Factor Optimization and 3D Scanner Capability Analysis. *RTe J.* **2024**. [CrossRef]
19. Giganto, S.; Martínez-Pellitero, S.; Cuesta, E.; Zapico, P.; Barreiro, J. Proposal of design rules for improving the accuracy of selective laser melting (SLM) manufacturing using benchmarks parts. *Rapid Prototyp. J.* **2022**, *28*, 1129–1143. [CrossRef]
20. Montero, J.; Weber, S.; Petroll, C.; Brenner, S.; Bleckmann, M.; Paetzold, K.; Nedeljkovic-Groha, V. Geometrical Benchmarking of Laser Powder Bed Fusion Systems Based on Designer Needs. *Proc. Des. Soc.* **2021**, *1*, 1657–1666. [CrossRef]
21. Maleki, E.; Salehnasab, B.; Paul, M.; Shao, S.; Shamsaei, N. Dimensional accuracy of fabricated geometries through powder bed fusion: An overview and a new benchmark artifact proposal. *Mater. Des.* **2025**, *257*, 114361. [CrossRef]
22. Rebaioli, L.; Fassi, I. A review on benchmark artifacts for evaluating the geometrical performance of additive manufacturing processes. *Int. J. Adv. Manuf. Technol.* **2017**, *93*, 2571–2598. [CrossRef]
23. Li, W.; Wang, K.; Fang, S. Benchmark Test Artifacts for Selective Laser Melting—A Critical Review. *Recent Pat. Eng.* **2022**, *16*, 76–86. [CrossRef]
24. de Pastre, M.-A.; Toguem Tagne, S.-C.; Anwer, N. Test artefacts for additive manufacturing: A design methodology review. *CIRP J. Manuf. Sci. Technol.* **2020**, *31*, 14–24. [CrossRef]
25. Moylan, S.; Slotwinski, J.; Cooke, A.; Jurrens, K.; Donmez, M.A. An Additive Manufacturing Test Artifact. *J. Res. Natl. Inst. Stand. Technol.* **2014**, *119*, 429–459. [CrossRef] [PubMed]
26. Castillo, L. *Study About the Rapid Manufacturing of Complex Parts of Stainless Steel and Titanium*; TNO Report with the Collaboration of AIMME; TNO: Hague, The Netherlands, 2005; pp. 1–31.
27. Yasa, E.; Kandemir, I.; Atik, I. On the Z-dimensional accuracy of L-powder bed fusion. *J. Addit. Manuf. Technol.* **2021**, *1*, 533. [CrossRef]
28. Sercombe, T.B.; Hopkinson, N. Process Shrinkage and Accuracy during Indirect Laser Sintering of Aluminium. *Adv. Eng. Mater.* **2006**, *8*, 260–264. [CrossRef]
29. Seifi, M.; Gorelik, M.; Waller, J.; Hrabe, N.; Shamsaei, N.; Daniewicz, S.; Lewandowski, J.J. Progress Towards Metal Additive Manufacturing Standardization to Support Qualification and Certification. *JOM* **2017**, *69*, 439–455. [CrossRef]
30. *ISO/ASTM 52902:2023*; Additive Manufacturing—Test Artefacts—Geometric Capability Assessment of Additive Manufacturing Systems. DIN Media GmbH: Berlin, Germany, 2023.
31. Elsevier—Scopus Document Search. Available online: https://www.scopus.com/search/form.uri?display=basic#basic (accessed on 18 July 2025).
32. Berez, J.; Praniewicz, M.; Saldana, C. Assessing laser powder bed fusion system geometric errors through artifact-based methods. *Procedia Manuf.* **2021**, *53*, 395–406. [CrossRef]
33. Carolo, L.C.B.; O, R.E.C.; de Oliveira, M.F.; Da Silva, J.V.L. The effects of varying wall thickness on the surface roughness of Ti-6Al-4V by electron beam powder bed fusion. *Surf. Topogr. Metrol. Prop.* **2023**, *11*, 35012. [CrossRef]
34. Krasniqi, M.; Löffler, F.; Tutsch, R. Influence of scanning strategies on dimensional accuracy in laser powder bed fusion. *Meas. Sens.* **2025**, *38*, 101840. [CrossRef]
35. Grabe, T.; Biermann, T.; Wolf, A.; Al-Nuwaider, J.; Krauss, H.; August, J.; Yu, W.; Heinz, J.B.; Bayerl, M.; Xu, K.; et al. Application-inspired additive manufacturing of Raman optics. *Opt. Laser Technol.* **2023**, *165*, 109574. [CrossRef]
36. Monzón, E.; Bordón, P.; Paz, R.; Monzón, M. Dimensional Characterization and Hybrid Manufacturing of Copper Parts Obtained by Atomic Diffusion Additive Manufacturing, and CNC Machining. *Materials* **2024**, *17*, 1437. [CrossRef]

37. Spitaels, L.; Rivière-Lorphèvre, E.; Demarbaix, A.; Ducobu, F. Adaptive benchmarking design for additive manufacturing processes. *Meas. Sci. Technol.* **2022**, *33*, 64003. [CrossRef]
38. Flierl, F.; Spies, B.C.; Rothlauf, S.; Vach, K.; Kohal, R.J.; Lüchtenborg, J. Effects of monomer contamination during post-rinsing in vat photopolymerization on dimensional stability. *Sci. Rep.* **2025**, *15*, 10139. [CrossRef]
39. ANSYS, Inc. Ansys Workbench | Simulation Integration Platform. Available online: https://www.ansys.com/products/ansys-workbench (accessed on 1 July 2025).
40. Nikon SLM Solutions. AlSi10Mg DIN EN 1706/EN AC-43000. Available online: https://www.slm-solutions.com/fileadmin/Content/Powder/MDS/nw/2024/MDS_AlSi10Mg_2024-04.1_EN.pdf (accessed on 2 June 2025).
41. *VDI 3405 Part 2.6*; Additive Manufacturing Processes—Powder Bed Fusion of Metal Using a Laser Beam (PBF-LB/M)—Presentation of Material Properties in Material Data Sheets. Beuth Verlag GmbH: Berlin, Germany, 2022.
42. Keyence. VL-550 3D Scanner. Available online: https://www.keyence.com/products/3d-measure/3d-scanner/vl/models/vl-550/ (accessed on 2 June 2025).
43. Keyence. VR-5200 3D-Profilometer. Available online: https://www.keyence.com/products/3d-measure/roughness-measure/vr-3000/models/vr-5200/ (accessed on 2 June 2025).
44. Dentaco. Induscan'Spray. Available online: https://www.dentaco.de/english-1/for-the-industry/indu-scan/ (accessed on 2 June 2025).
45. *ISO 286-1:2019-09*; Geometrical Product Specifications (GPS), ISO Code System for Tolerances on Linear Sizes: Part 1: Basis of Tolerances, Deviations and Fits. Beuth Verlag GmbH: Berlin, Germany, 2019.
46. Silva, E.C.; Lopes, A.C.; Sampaio, Á.M.; Pontes, A.J. Influence of layer thickness on dimensional and geometrical properties of aluminium parts produced by powder bed fusion. *Int. J. Adv. Manuf. Technol.* **2025**, *138*, 4755–4766. [CrossRef]
47. Lu, Y.; Badarinath, R.; Lehtihet, E.A.; de Meter, E.C.; Simpson, T.W. Experimental sampling of the Z-axis error and laser positioning error of an EOSINT M280 DMLS machine. *Addit. Manuf.* **2018**, *21*, 501–516. [CrossRef]
48. Yang, P.; Deibler, L.A.; Bradley, D.R.; Stefan, D.K.; Carroll, J.D. Microstructure evolution and thermal properties of an additively manufactured, solution treatable AlSi10Mg part. *J. Mater. Res.* **2018**, *33*, 4040–4052. [CrossRef]
49. Lubis, D.Z.; Aminnudin, A.; Perwira, A.H. Punch Tool Speed and Material Effect on Keychain Cranioplasty Plate Dimensions Using Finite Element Method. *Key Eng. Mater.* **2020**, *851*, 105–110. [CrossRef]
50. Yasa, E.; Deckers, J.; Craeghs, T.; Badrossamay, M.; Kruth, J.-P. Investigation on Occurrence of Elevated Edges in Selective Laser Melting. In Proceedings of the International Solid Freeform Fabrication Symposium, Austin, TX, USA, 3–5 August 2009; University of Texas at Austin: Austin, TX, USA, 2009.
51. Matache, G.; Vladut, M.; Paraschiv, A.; Condruz, R.M. Edge and corner effects in selective laser melting of IN 625 alloy. *Manuf. Rev.* **2020**, *7*, 8. [CrossRef]
52. Pant, M.; Patpatiya, P.; Nagdeve, L.; Moona, G.; Kumar, H. Reverse Engineering and Dimensional Limits Analysis of Samples Fabricated Using Selective Laser Melting Process. *Mapan—J. Metrol. Soc. India* **2023**, *38*, 795–804. [CrossRef]
53. Calignano, F.; Galati, M.; Iuliano, L. A Metal Powder Bed Fusion Process in Industry: Qualification Considerations. *Machines* **2019**, *7*, 72. [CrossRef]
54. Brenner, S.; Moser, M.; Strauß, L.; Nedeljkovic-Groha, V.; Löwisch, G. Recoater crashes during powder bed fusion of metal with laser beam: Simulative prediction of interference and experimental evaluation of resulting part quality. *Prog. Addit. Manuf.* **2023**, *8*, 759–768. [CrossRef]
55. Craeghs, T.; Clijsters, S.; Yasa, E.; Kruth, J.-P. Online Quality Control of Selective Laser Melting. In Proceedings of the 20th Solid Freeform Fabrication (SFF) Symposium, Austin, TX, USA, 8–10 August 2011; pp. 212–226.
56. Morvayova, A.; Fabbiano, L.; Contuzzi, N.; Caiazzo, F.; Casalino, G. On the influence of building position on dimensional accuracy and surface quality of aluminum blocks manufactured by L-PBF. *Opt. Laser Technol.* **2023**, *167*, 109830. [CrossRef]
57. Afazov, S.; Denmark, W.A.; Lazaro Toralles, B.; Holloway, A.; Yaghi, A. Distortion prediction and compensation in selective laser melting. *Addit. Manuf.* **2017**, *17*, 15–22. [CrossRef]
58. Strumza, E.; Yeheskel, O.; Hayun, S. The effect of texture on the anisotropy of thermophysical properties of additively manufactured AlSi10Mg. *Addit. Manuf.* **2019**, *29*, 100762. [CrossRef]
59. *ISO/ASTM/TS 52930:2021*; Additive Manufacturing—Qualification Principles—Installation, Operation and Performance (IQ/OQ/PQ) of PBF-LB Equipment. DIN Media GmbH: Berlin, Germany, 2021.
60. Mehdi-Souzani, C.; Piratelli-Filho, A.; Anwer, N. Comparative Study for the Metrological Characterization of Additive Manufacturing artefacts. In *Advances on Mechanics, Design Engineering and Manufacturing. Lecture Notes in Mechanical Engineering*; Eynard, B., Nigrelli, V., Oliveri, S., Peris-Fajarnes, G., Rizzuti, S., Eds.; Lecture Notes in Mechanical Engineering; Springer: Cham, Germany, 2017.
61. Patuelli, C.; Cestino, E.; Frulla, G.; Valente, F.; Servetti, G.; Esposito, F.; Barbero, L. FEM Simulation of AlSi10Mg Artifact for Additive Manufacturing Process Calibration with Industrial-Computed Tomography Validation. *Materials* **2023**, *16*, 4754. [CrossRef] [PubMed]

62. Xie, D.; Lv, F.; Liang, H.; Shen, L.; Tian, Z.; Zhao, J.; Song, Y.; Shuai, C. Towards a comprehensive understanding of distortion in additive manufacturing based on assumption of constraining force. *Virtual Phys. Prototyp.* **2021**, *16*, S85–S97. [CrossRef]
63. Brenner, S.; Nedeljkovic-Groha, V. Distortion Compensation of Thin-Walled Parts by Pre-Deformation in Powder Bed Fusion with Laser Beam. In *Lectures Notes on Advanced Structured Materials 2*; Altenbach, H., Hitzler, L., Johlitz, M., Merkel, M., Öchsner, A., Eds.; Springer International Publishing AG: Cham, Switzerland, 2024; pp. 205–219, ISBN 978-3-031-49042-2.
64. Taylor, H.C.; Garibay, E.A.; Wicker, R.B. Toward a common laser powder bed fusion qualification test artifact. *Addit. Manuf.* **2021**, *39*, 101803. [CrossRef]